Accepted for publication in the Astrophysical Journal

ISO-SWS spectroscopy of NGC 1068 [1]

D. Lutz[2], E. Sturm[2], R. Genzel[2], A.F.M. Moorwood[3], T. Alexander[4], H. Netzer[5], A. Sternberg[5]

ABSTRACT

We present ISO-SWS spectroscopy of NGC 1068 for the complete wavelength range 2.4 to 45μm at resolving power ~1500. Selected subranges have been observed at higher sensitivity and full resolving power ~2000. We detect a total of 36 emission lines and derive upper limits for 13 additional transitions. Most of the observed transitions are fine structure and recombination lines originating in the narrow line region (NLR) and the inner part of the extended emission line region.

We compare the line profiles of optical lines and reddening-insensitive infrared lines to constrain the dynamical structure and extinction properties of the narrow line region. The most likely explanation of the considerable differences found is a combination of two effects. (1) The spatial structure of the NGC 1068 narrow line region is a combination of a highly ionized outflow cone and lower excitation extended emission. (2) Parts of the narrow line region, mainly in the receding part at velocities above systemic, are subject to extinction that is significantly suppressing optical emission from these clouds. Line asymmetries and net blueshifts remain, however, even for infrared fine structure lines suffering very little obscuration. This may be either due to an intrinsic asymmetry of the NLR, as perhaps also suggested by the asymmetric radio continuum emission, or due to a very high column density obscuring component which is hiding part of the narrow line region even from infrared view.

We present detections and limits for 11 rotational and ro-vibrational emission lines of molecular hydrogen (H_2). They arise in a dense molecular medium at temperatures of a few hundred Kelvin that is most likely closely related to the warm and dense components seen in the near-infrared H_2 rovibrational transitions, and in millimeter

---

[1]Based on observations with ISO, an ESA project with instruments funded by ESA Member States (especially the PI countries: France, Germany, the Netherlands and the United Kingdom) with the participation of ISAS and NASA.

[2]Max-Planck-Institut für extraterrestrische Physik, Postfach 1603, 85740 Garching, Germany

[3]European Southern Observatory, Karl-Schwarzschild-Straße 2, 85748 Garching, Germany

[4]Institute for Advanced Study, Olden Lane, Princeton, NJ 08540, USA

[5]School of Physics and Astronomy and Wise Observatory, Raymond and Beverly Sackler Faculty of Exact Sciences, Tel Aviv University, Ramat Aviv, Tel Aviv 69978, Israel

wave tracers (CO, HCN) of molecular gas. Any emission of the putative pc-scale molecular torus is likely overwhelmed by this larger scale emission.

In companion papers we use the SWS data to derive the spectral energy distribution emitted by the active nucleus of NGC 1068 (Alexander et al. 2000), to put limits on infrared emission from the obscured broad line region (Lutz et al. 2000), and discuss the continuum and its features in conjunction with SWS spectra of other galaxies (Sturm et al. 2000).

Subject headings: galaxies: individual (NGC 1068) — galaxies: Seyfert— infrared: ISM: lines and bands

1. Introduction

NGC 1068 is one of the nearest and probably the most intensely studied Seyfert 2 galaxy. Observations in all wavelength bands from radio to hard X-rays have formed a uniquely detailed picture of this object. NGC 1068 has played a key role in the development of unified scenarios for Seyfert 1 and Seyfert 2 galaxies (Antonucci & Miller 1985), in the study of molecular gas in the nuclear region of Seyferts (e.g. Myers & Scoville 1987; Tacconi et al. 1994), and in elucidating the importance of star formation activity coexistent with the AGN, both on larger (e.g. Telesco & Decher 1988) and smaller (Macchetto et al. 1994; Thatte et al. 1997) scales. NGC 1068 hosts a prominent Narrow Line Region (NLR) that is approximately cospatial with a linear radio source with two lobes (Wilson & Ulvestad 1983). The narrow emission line region has been extensively characterized from subarcsecond clouds probed by HST (Evans et al. 1991; Macchetto et al. 1994), the ≈ 5 arcseconds of the NLR hosting most of the line flux (e.g. Walker 1968; Shields & Oke 1975; Cecil et al. 1990), and the ionization cone and extended emission line region (Pogge 1988; Unger et al. 1992) extending to radii of at least $30''$ ($1'' = 72$ pc at the distance of 14.4 Mpc, Tully 1988). The velocity field is complex, with an ensemble of rapidly moving clouds dominating the inner arcseconds and a more quiescent rotation pattern prevailing at larger radii (e.g. Walker 1968; Alloin et al. 1983; Meaburn & Pedlar 1986; Cecil et al. 1990). While most of the excitation of the narrow line region and the extended emission line region is likely through photoionization by the central AGN (Marconi et al. 1996), high resolution observations suggest kinematic disturbance and possibly shock excitation of regions close to the radio outflow (e.g. Axon et al. 1998).

With ESA's *Infrared Space Observatory* ISO, sensitive mid-infrared spectroscopy of AGNs became possible, with detections of a broad range of low- and high-excitation fine structure lines, recombination lines, and pure rotational lines from such sources (Moorwood et al. 1996; Sturm et al. 1999; Alexander et al. 1999)). Model predictions of the mid-IR spectra of AGN had been obtained prior to ISO (e.g. Spinoglio & Malkan 1992), but observations were restricted by limited sensitivity and focussed primarily on the continuum emission and broad features rather than emission lines.

In this paper, we present the ISO-SWS spectra of NGC 1068 and draw conclusions on the structure of the narrow line region that can be obtained mainly from the comparison of optical and reddening-insensitive infrared lines, and discuss the nature of the mid-infrared molecular hydrogen emission. The ISO-SWS data of NGC 1068 are analysed further in several companion papers. Alexander et al. (2000) use photoionization modelling based on the ISO fine structure line set and other NLR lines to model the shape of the AGN's spectral energy distribution. Lutz et al. (2000) analyze limits on emission from the obscured broad line region. Finally, Sturm et al. (2000) discuss continuum energy distribution and features of NGC 1068 in conjunction with ISO-SWS spectra of other galaxies.

Our paper is organised as follows. In §2 we discuss the ISO-SWS observations and data reduction. §3 presents results and implications of the density of the narrow line region. §4 uses infrared line profiles in comparison to optical ones to constrain the structure of the narrow line region. We discuss the mid-infrared molecular hydrogen emission in §5 and summarize in §6.

2. Observations and data reduction

We have used the Short Wavelength Spectrometer SWS (de Graauw et al. 1996) on board the *Infrared Space Observatory* ISO (Kessler et al. 1996) to observe the nuclear region of NGC 1068. In Table 1 we present a log of our observations. We carried out observations in the SWS01 mode which provides a full 2.4 – 45μm scan at slightly reduced spectral resolving power, as well as observations in the SWS02 and SWS06 modes targeted at full resolution observations of individual lines or short ranges. Because of the large width of the emission lines in the NGC 1068 narrow line region, we have mostly relied on the SWS06 mode which can be set up to provide wider continuum baselines than standard SWS02 line scans. We supplement observations from our ISO guaranteed and open time with serendipitous information on some fine structure lines obtained in another ISO project (PI G. Stacey), the main results of which are to be presented elsewhere.

Table 1 includes also the position angle of the long axis of the SWS apertures for the various observations. Our pointing was always centered on the nucleus of NGC 1068, but the SWS apertures range from $14''\times20''$ at short wavelengths to $20''\times33''$ at the longest wavelengths (de Graauw et al. 1996). At the long wavelengths, we partly include the $\sim$15$''$ radius ring of star forming regions encircling the nucleus of NGC 1068. The apertures were always oriented in approximately north-south (or south-north) direction, with position angles between -11° and -23°.

We have analyzed the data using the SWS Interactive Analysis (IA) system (Lahuis et al. 1998; Wieprecht et al. 1998) and calibration files of July 1998. A preliminary account of part of the observations is given by Lutz et al. (1997). Since then, calibration files have been updated for wavelength calibration and in particular with respect to the SWS relative spectral response function, leading to more reliable intercalibration between the 'AOT bands' forming a full SWS spectrum. Our data reduction started in the standard way and continued with steps of (interactive) dark current subtraction and matching up- and downscans. We eliminated data from those detectors of band 3 that were most noisy during a particular revolution, and from interactively identified regions with single detector signal jumps in bands 1 and 2, and simultaneous 12-detector signal jumps in band 3. After relative spectral response correction and flux calibration, we 'flatfielded' the 12 detectors of a band to a consistent level, corrected for the ISO velocity, and extracted the AAR data product. Redundant scans of the same line were shifted to a consistent level. Single-valued spectra were produced by kappa-sigma clipping the AAR dot cloud and rebinning it with a resolution of typically 3000 which does not lead to significant smearing for NGC 1068 linewidths. For those ranges affected by fringes, the single-valued spectra were defringed using the iterative sine fitting option of the aarfringe module within the SWS Interactive Analysis.

The large number of observations required special treatment of redundant data. In addition, observations from revolution 285 where apparently affected by a slight ($\approx 2 - 3''$?) pointing problem, which occured occasionally in the earlier phase of the ISO mission. Since SWS beam profiles in some AOT bands are peaked and slightly offset with respect to the nominal pointing (A. Salama, 1999, priv. comm.), modest pointing offsets can cause noticeable flux losses in some AOT bands and resulting band mismatches. Such mismatches were evident in revolution 285 band 3 data. Since most of the NGC 1068 mid-infrared flux comes from a small region (Cameron et al. 1993; Braatz et al. 1993; Bock et al. 1998), we corrected for this problem and the small scatter between other observations by the following scaling procedure: For the SWS01 full spectrum obtained in revolution 285, the individual AOT bands were scaled to obtain both good match at band limits, and good agreement with the overall flux level as estimated from our other SWS data and ground-based photometry (Lebofsky et al. 1978; Rieke & Low 1975). At wavelengths below 10μm photometry from different epochs should be used with great caution because of the known variability (Glass 1997), our fluxes are however in good agreement with the photometry of Glass for the ISO epoch. All other data were then scaled to this SWS01 spectrum by the ratio inferred from the continuum flux densities. We believe the final flux scale to be accurate within the 20-30% typical for SWS data (Schaeidt et al. 1996).

Accurate wavelength calibration of the SWS grating spectrometer is central for part of our line profile analysis, since shifts between lines in NGC 1068 tend to be of the order 300 km/s or less (Marconi et al. 1996). Valentijn et al. (1996) deduce an accuracy of $\sim$30km/s from extensive calibrations during the SWS performance verification phase. Since then, a slow secular drift in SWS wavelength calibration has been calibrated to similar accuracy. We have tested the wavelength calibration of the NGC 1068 data, using identical calibration files to analyze spectra of the planetary nebulae NGC 7027 and NGC 6543 taken close to revolution 633 where some of the most important NGC 1068 lineprofiles were taken. We confirm the excellent accuracy from these observations, the largest error not exceeding the value given by Valentijn et al. (1996). This test and the good internal consistency of velocities measured in NGC 1068 for different lines from the same species spanning most of the SWS wavelength range (e.g. H_2, see Table 2) leads us to adopt an upper limit of 50 km/s for any systematic errors in our wavelength scale, taking into account a margin for mispointing.

Two emission features, which were tentatively detected in the preliminary analysis of Lutz et al. (1997) could not be confirmed with the larger observational database and the improved calibration. A broad emission feature near 19μm, which might be interpreted as silicate emission, is not confirmed with the new spectral response calibration. An emission line at 28μm was identified as an unusually strong H_2 S(0) line. This identification was later found suspect because of the line's larger width compared to the other H_2 lines observed in NGC 1068. The line was not confirmed in deeper follow up observations. Detailed inspection of the original data indeed shows that it is an artifact of a highly unlikely coincidence of detector 'glitches' at the expected wavelength of the S(0) transition.

3. Results

The 2.4-45μm full spectrum of NGC 1068 is displayed in Figure 1. Some solid state features are superposed on the strong AGN-heated mid-infrared continuum. These include 3.4μm C-H absorption, 9.6μm silicate absorption, and 7.7, 8.6, 11.3μm 'PAH' emission (see Sturm et al (2000) for a discussion in conjunction with other SWS spectra of galaxies). Bright fine structure emission lines, mainly originating in the narrow line region, are already visible in the full spectrum. Figures 2 and 3 show individual emission lines. The display range is chosen to be $\pm$2500 km/s around systemic velocity for recombination and fine structure lines, and $\pm$1000 km/s for the much narrower molecular lines. Throughout this paper, we adopt a systemic velocity of 1148km/s (Brinks et al. 1997). Good rest wavelengths are available for the observed transitions from the literature and from recent ISO determinations (Feuchtgruber et al. 1997). Many lines were observed repeatedly, Figures 2 and 3 show only the best quality data. Table 2 lists the measured line fluxes and limits, presenting averages of independent measurements with higher weight given to better data. Table 2 includes also upper limits for some transitions (not shown in Figure 2) that were observed with good enough signal-to-noise ratio. We list such limits for transitions from elements like Na or Ar where other ionization stages are detected.

Fluxes of relatively narrow lines, for example from H_2 and [Si II], were measured by direct integration of the continuum subtracted line profiles. The large linewidth makes this procedure error prone for faint lines from the NLR, where continuum definition is the main source of measurement error. The relative constancy of NLR line profiles over a wide range of lower ionization potentials (see below) lead us to adopt a different procedure to measure fluxes for the NLR lines: We derived a simple two-gaussian template from the brightest NLR lines ([O IV] 25.89μm (note nearby [Fe II]), [Ne V] 24.32μm, [Ne VI] 7.652μm) and used fits of this template (Figure 4) plus a linear continuum to measure the fluxes of fainter NLR lines. The two gaussian components have FWHM 333 and 1246 km/s, peak ratio narrow/wide 1.34, and the wider component is blueshifted by 100km/s. In fitting, we varied only continuum flux and slope, total line flux, and total velocity. The fluxes measured this way agreed very well ($\lesssim$10%) with those determined by direct integration not only for the lines used to derive the template, but also for other bright NLR lines like [Mg VIII] 3.028μm. The fit thus preserves the fluxes for bright lines and is preferable for faint lines where continuum subtraction is the dominant source of error.

For the blended lines of [Mg VII] and H_2 (0-0) S(7) near 5.5μm, we list the fluxes resulting from a tentative gaussian fit using two components for [Mg VII] and one component for H_2. The uncertainty of the S(7) flux is particularly large, up to a factor 2. The H_2 excitation diagram (Figure 9) in fact suggests that it may be overestimated. Similar caution has to be applied to the tentative flux listed for the [Fe II] 25.99μm line. A slight shoulder appears in the long wavelength wing of the [O IV] 25.89μm transition, but its flux is very uncertain and may at best be good enough to serve for consistency checks with other [Fe II] lines. Feuchtgruber et al. (1997) discuss evidence that the lines of [Ar III] and [Mg VII] at 9.0μm are blended at the resolution of SWS. We list only a total flux in Table 2.

We detect a weak unidentified feature at rest wavelength about 7.555μm. If real, its width would suggest a NLR origin. An instrumental origin due to an imperfection of the relative spectral response function (RSRF) cannot be excluded but is unlikely since the RSRF shows very little structure at that wavelength. Also, instrumental 'ghosts' to strong SWS lines are not known at such a level. A possible interpretation of this feature is that it is a blueshifted ($\sim$3800 km/s) component of the nearby strong [Ne VI] line containing $\sim$1.5% of the total line flux. Residual instrumental fringing prevents us from looking for analogous components near other strong lines such as [Ne V] or [O IV]. At this point, the feature must be considered as possibly real but without an obvious identification by a line that is potentially strong in AGN spectra. Also, no line is seen at this wavelength in archival ISO spectra of the high excitation planetary nebula NGC 6302.

We postpone a detailed discussion of the line profiles to section 4. Figures 2 and 3 already suggest, however, that we are dealing with three distinct components: Fine structure transitions from species with lower ionization potential $\gtrsim$ 40 eV (i.e. from [Ne III] upwards) have similar wide profiles and apparently originate in the NLR. Fine structure lines from lower ionization stages, in particular [Ne II] and [S III], are narrower and are most likely contaminated by star formation within their beams. This limits their use in modelling of the AGN-excited NLR spectrum (Alexander et al. 2000) to upper limits rather than measurements. Inspection of Figure 2 suggests that the starburst contribution strongly dominates the low excitation lines like [S III] 33.48μm and [Si II] 34.81μm which are measured with the largest aperture. Lines measured with intermediate apertures like [Ne II] 12.81μm and in particular [S III] 18.71μm still show strong wings and will have a considerable NLR contribution. The smallest line widths are measured for transitions of molecular hydrogen.

3.1. Density of the narrow line region

The fine structure lines detected by SWS can be used to determine the density and, in conjunction with optical forbidden lines, the electron temperature of the line emitting gas in the narrow line and coronal line regions. Differences in infrared and optical lineprofiles (§4) discourage a determination of electron temperatures from the integrated fluxes, which would not account for significant variations in extinction across the NLR. A reliable average density can be determined, however, from the mid-infrared lines alone which are insensitive to electron temperature and extinction variations. The contribution of starburst excitation to the density-sensitive forbidden lines can be estimated using the large line width variation between the NLR and the circumnuclear ring of star formation regions.

The most suitable NLR density diagnostic is provided by the ratio of the [Ne V] transitions at 14.32 and 24.32μm. These lines cannot be diluted significantly by circumnuclear star formation since they are undetected in starburst galaxies (Genzel et al. 1998). They were observed with the same SWS aperture size and with good signal-to-noise. Adopting the same atomic data as Alexander et al. (1999, see also their Figure 3 for diagrams of several density sensitive ratios) and an electron temperature of 10000 K, the observed [Ne V] ratio of 1.39 corresponds to an electron density $n_e \sim 2000\,cm^{-3}$ in the region of the NLR where species with lower ionization potential near 100eV prevail.

A seemingly discrepant result is obtained from the [S III] transitions at 18.71 and 33.48μm – the observed ratio of 0.73 is consistent with the low density limit and corresponds to $n_e \lesssim 500\,cm^{-3}$. But, Figure 2 shows the line profiles of the two transitions to be quite different: [S III] 18.71μm shows strong wide wings and is apparently NLR-dominated with small starburst contamination. In contrast, the larger aperture of [S III] 33.48μm collects more emission from the starburst ring showing up as a strong narrow component of the profile. If *all* 18.71μm emission were from a NLR at $2000\,cm^{-3}$, the NLR contribution to the 33.48μm flux would be about 1/3, consistent with the weaker wings of this line.

A similar problem may affect, to a lesser degree, the density sensitive ratio of the [Ne III] transitions at 15.55 and 36.01μm. The observed ratio of 8.9 is lower than but probably still consistent with the low density limit ($\sim$12) which applies up to the $n_e \sim 2000\,cm^{-3}$ derived from [Ne V]. The modest signal-to-noise ratio of the 36.01μm line makes it impossible to use the line profile to assess starburst contamination in the large aperture. A crude estimate can be obtained assuming that the ratio of *starburst* [Ne III] 36.01μm and [S III] 33.48μm seen additionally in the large aperture is 0.03–0.04 as in the prototypical starburst M 82 (Förster-Schreiber 1998). Then, $\gtrsim$10% of the 36.01μm line would be starburst contamination, bringing the ratio closer to its low density limit value. The density in NLR regions dominated by lower excitation species like [S III] and [Ne III] hence appears consistent with that for the higher excitation region containing [Ne V].

With respect to the coronal line region, the observed ratio 0.55 of the [Si IX] lines at 2.584 and 3.936μm is close to its low density limit which implies $n_e \lesssim 10^6\,cm^{-3}$. The same limit is found for the Circinus galaxy (Moorwood et al. 1996) and NGC 4151 (Sturm et al. 1999). Such a density limit is consistent with all popular scenarios for coronal line formation in AGN except for origin in a very dense transition region between NLR and BLR.

4. Line profiles and the structure of the narrow line region

Integrated emission lines profiles are an indirect tool to constrain the dynamical structure and extinction properties of the narrow line region. Different lines probe different parts of the NLR and the velocity field is generally far from uniform. With the advent of linear optical detectors, considerable effort was devoted to studies of both forbidden and permitted optical line profiles in Seyfert galaxies. Although there is still no full consensus among different studies of the NLR forbidden lines, the emerging picture is as follows.
(1) The forbidden lines in most cases show blue asymmetries in the sense of a sharper falloff to the red than to the blue. Line centroids are blueshifted with respect to the systemic velocity, whereas line peaks in high resolution spectra are close to systemic velocity. This has been most thoroughly studied in moderate excitation species including [O III] 5007Å (e.g. Heckman et al. 1981; Vrtilek & Carleton 1985; Whittle 1985a; Dahari & De Robertis 1988) but holds also for the higher excitation coronal lines (Penston et al. 1984).
(2) Line widths and blueshifts often vary between different species observed in the same source. Line profiles appear to be correlated with the ionization potential and/or the critical density. There are indications, but no complete consensus, that the correlation with the critical density may be the fundamental one (e.g. Pelat et al. 1981; Penston et al. 1984; Whittle 1985b; De Robertis & Osterbrock 1986; Appenzeller & Östreicher 1988).

Various scenarios have been put forward to explain these trends. Most of them invoke extinction to explain blue asymmetries, and the most popular ones assume outflow in a dusty NLR, with higher excitation species probably originating closer to the central source in regions of higher velocity and obscuration. It is obvious that observations of *infrared* NLR emission are a powerful independent method to test such scenarios: near- and mid- infrared lines suffer more than an order of magnitude less extinction than in the optical. The combination of optical and infrared data should hence elucidate the role of dust obscuration. Comparison of recombination line profiles in the optical with infrared ones would be advantageous because of the relative insensitivity of recombination line emissivities to local gas conditions. The line-to-continuum ratio of recombination lines in the infrared is low, however, and better profiles are obtained for coronal and fine structure lines which additionally cover a wide range of excitations. Sturm et al. (1999) have presented a first such analysis using ISO-SWS observations of NGC 4151. On the basis of the similarity of optical and infrared profiles, they ruled out the most simple scenario of an outflowing NLR with pervasive dust, and suggested either a geometrically thin but optically highly thick obscuring disk, or an intrinsic asymmetry of the NLR.

Because of the large flux and width of its 'narrow' lines, NGC 1068 is best suited for a line profile analysis at the modest resolving power (∼2000) of ISO-SWS. Optical line profiles have been observed at very high resolving power by various groups (e.g. Pelat & Alloin 1980; Alloin et al. 1983; Meaburn & Pedlar 1986; Veilleux 1991; Dietrich & Wagner 1998) and show complex, multi-peaked structure related to individual cloud complexes within the narrow line region of NGC 1068. Marconi et al. (1996) have extended this work into the near infrared. At lower resolving power, they do not discriminate the fine details of the best optical profiles but derive the line centroids by Gaussian fits for a large set of near-infrared and optical lines. They find that all optical and near-infrared high excitation lines are significantly blueshifted with respect to systemic velocity (>200km/s for lower ionization potential $\gtrsim$ 20eV). They interpret this significant trend as a consequence of non-isotropic flows or ionization patterns rather than selective extinction effects.

We extracted line profiles for five high signal-to-noise SWS lines by subtracting a linear continuum fitted outside 2500km/s from the line center and normalizing to the peak of the line. These five lines originate in species spanning a wide range of excitation potentials ranging from 55 to 303eV and are shown in Figure 4. The remaining uncertainty of these profiles is dominated by noise for the high excitation lines of [Mg VIII] and [Si IX] and by continuum uncertainties for the other lines. These could be both due to weak underlying real continuum features (e.g. PAH near [Ne VI]) and due to residual fringing ([Ne V] and [O IV]). We do not show low excitation lines with significant starburst contribution, and the [Ne V] 14.32μm and [Ne III] 15.55μm lines which are consistent with those shown in Figure 4 but more uncertain due to fringing. Brackett α has a much lower line to continuum ratio but still good signal-to-noise ratio, and a line profile similar to the fine structure lines, as discussed by Lutz et al. (2000) in the context of putting limits on a broad line region contribution.

For lines too faint to derive a good line profile, we fitted a single gaussian plus linear continuum to derive at least a centroid velocity (Table 2). While such a gaussian is not a good approximation to the intrinsic NLR profile, we adopted it for simplicity and for consistency with the optical/near-infrared data of Marconi et al. (1996). We also fitted the two-component NLR profile of Figure 4 but do not list the derived velocities since they agree with the simple gaussian fit except for an offset that is constant within the uncertainties. From repeated observations for some of these lines, we estimate an error of $\lesssim$50km/s. For lines with no velocity listed in Table 2, we estimate that the uncertainty of deriving the centroid of a broad noisy line is too large to include it into an analysis of NGC 1068. None of them, however, is discrepant by more than ≈300km/s which would suggest misidentification.

In the following subsections, we will derive a large aperture optical NLR line profile for comparison with the ISO data, compare optical and infrared profiles and centroid velocities, and interpret the differences found.

4.1. A large aperture optical line profile

Mismatch between the typically small optical apertures and the large mid-IR ones is important when attempting to compare optical and mid-IR line profiles. Datacubes from imaging spectroscopy would be ideal to extract optical line profiles matching the ISO apertures. At this point, however, published imaging spectroscopy of NGC 1068 is either limited in field size (Pécontal et al. 1997) or lacks wavelength coverage: The datacube of Cecil et al. (1990) has been obtained with 2600km/s total coverage in the [N II] lines that are additionally heavily blended with Hα, making it difficult to determine the extent to which broad components are missing in their total line profile (their Fig. 7).

We make use of two auxiliary large aperture optical spectra to address the problem of aperture mismatch: A 4000 to 7800Å spectrum from Wise Observatory (WO, S. Kaspi 1999, priv. communication), providing good fluxes of the brightest lines in a $10'' \times 15''$ aperture (position angle 0°), and a high spectral resolution Coudé Echelle spectrum from Karl Schwarzschild Observatory Tautenburg (KSO, E. Guenther 1999, priv. communication), providing a good [O III] line profile (though not good fluxes) in a $6.8'' \times 15''$ aperture (mean position angle -28°, varying during integration). In addition, we estimated relative emission line fluxes in our apertures by integrating over the corresponding regions of a narrow band [O III] map (R. Pogge, M.M. deRobertis, 1999, unpublished data). Both the Wise spectrum and the [O III] map confirm that ISO line fluxes of the NGC 1068 NLR can be sensibly compared to smaller aperture optical data, since those already sample most of the flux in the narrow line region. For example, a $4''$ diameter aperture will already get $\approx$70% of the flux in the ISO aperture. The fluxes measured in the large Wise aperture for the brightest optical lines agree within $\sim$30% with published smaller aperture ones (e.g. Shields & Oke 1975; Koski 1978; Marconi et al. 1996).

Figure 5 displays our KSO $6.8'' \times 15''$ aperture [O III] 5007Å line profile in comparison to its $2.5'' \times 2.5''$ equivalent (Veilleux 1991). The line profile changes induced by this more than tenfold increase in aperture area are relatively modest and fit expectations from high resolution longslit spectroscopy. While the major components of Veilleux' spectrum are well reproduced in the KSO data, their ratios differ somewhat leading to an overall slightly wider profile. This is fully consistent with observations of relatively broad components over larger regions not sampled by Veilleux' aperture (Pelat & Alloin 1980; Alloin et al. 1983; Meaburn & Pedlar 1986). The only feature in the KSO profile not present in the Veilleux profile is an additional narrow feature at or slightly redshifted from systemic velocity. This feature almost certainly corresponds to the 'velocity spike' in the NE region of the NLR detected by many authors but seen perhaps most clearly in the data of Meaburn & Pedlar (1986). This feature is missed by Veilleux' aperture but partly covered by the KSO data.

The KSO aperture is still about three times smaller in area than the SWS apertures through which the best fine structure line profiles have been taken. The drop in [O III] surface brightness with radius is so rapid (e.g. Fig. 1 of Meaburn & Pedlar 1986) that only modest differences in the total line profile are expected. An exception to this is the NE region of the NLR about 6″ from the nucleus which was incompletely covered. The KSO slit orientation cannot be chosen freely and was approximately aligned with the ISO apertures but not with the NLR (PA -28° instead of PA ≈30°), missing part of the NE end of the NLR. Long slit spectroscopy (e.g. Meaburn & Pedlar 1986) shows this NE region to be dominated by the narrow 'velocity spike' near systemic velocity which is already seen in the comparison of KSO and Veilleux (1991) profiles. We hence expect this spike to be more prominent in an optical line profile fully equivalent to the ISO aperture. Integrating the [O III] map over the ISO and KSO apertures we estimate a need to add ∼11% to the KSO flux to account for the NE region and other low surface brightness emission near systemic velocity. We have taken this into account by adding such a narrow (FWHM 150km/s) component to the KSO profile, and will use this in the following as basis of our optical line profile comparison (see also Figure 5). Use of such a modified profile is supported by the spectrum of Pelat & Alloin (1980) which was obtained with a rotating longslit sweeping across the NE region of the NLR, and showing a similar narrow spike (their component 5).

4.2. Line profile variations

The optical and infrared line profiles in NGC 1068 differ strongly. This is most evident in Figure 6 which compares the profiles of [O IV] 25.89μm and [O III] 5007Å. We chose [O IV] as the representative infrared line since it was observed with very good S/N and is close to [O III] in lower ionization potential of the emitting species (55 vs. 35eV), ensuring origin in a similar region of the NLR. Critical densities ($1.0 \times 10^4\,\mathrm{cm}^{-3}$ vs. $7.0 \times 10^5\,\mathrm{cm}^{-3}$) match less well than [Ne V] or [Ne VI] would, but this is less relevant given the low NLR density we have inferred (see §3.1).

The optical [O III] line profile is both blueshifted and broader than the infrared [O IV] line profile. There are however also significant similarities. Shoulders near -900 km/s and ∼350 km/s are present in both profiles. Adopting different relative scalings (Figure 6), the impression arises that the two profiles in fact agree fairly well over parts of their extent if the scaling is set properly. The main difference lies in *different relative strengths of blue wing, center, and red wing*, the infrared profile having a stronger red wing and center.

The four highest quality infrared profiles are compared in Figure 7 using a spread velocity scale. The most obvious and significant variation is in [Mg VIII] which is both broader and more blueshifted than the lower excitation lines. The same is observed for the more noisy [Si IX] line. As already noted, the [O IV],[Ne V], and [Ne VI] profiles with excitation energies ranging from 55 to 126eV are very similar but the overplot shows some variation in detail. There is a minor shift in the narrow core of the [Ne VI] line which is, however, not significant compared to the quoted systematic uncertainty. Comparing [Ne V] to [O IV] taken from the same observation there is even less shift. Concerning the broader wings, there are significant differences in addition to the possible presence of [Fe II] at ≈1100km/s in the [O IV] profile. There is a trend from [O IV] to [Ne VI] in the blue wing becoming stronger and the red wing fainter.

Such profile variations determine the line centroids derived from gaussian fits (Table 2) to which we add a centroid of 1015 km/s derived in the same way for our extrapolated large aperture optical [O III] profile. Anticipating that the shifts may reflect several partially degenerate influences, we show in Figure 8 centroid velocities as a function of lower ionization potential, critical density, and extinction for the particular line. The extinction values are relative and based on a preliminary ISO-based extinction curve for the center of our Galaxy (Lutz et al. 1997a).

The trend observed in the ISO data for the velocity centroids as a function of ionization potential (Figure 8) is markedly different from the equivalent dataset obtained in the optical and near-infrared (Figure 8, data taken from Marconi et al. 1996). In both data sets the velocity centroids of the lowest excitation non-NLR lines (H_2, [Fe II]) are close to systemic. However, none of the ISO lines reach the large blueshifts observed consistently over a wide excitation range in the optical and near-infrared. The data sets are least discrepant at the high excitation end. Here, [Si IX] 3.936μm is common to both sets and agrees within the errors, though being somewhat less blueshifted in the ISO data. The discrepancy is largest at intermediate excitation (20-200eV) where the optical/NIR lines are all strongly blueshifted while the ISO lines only slowly deviate from systemic velocity as excitation increases.

4.3. Interpretation of the profile differences

In addition to the cloud distribution and kinematics, line profiles reflect the emissivities of fine structure or forbidden lines in the narrow line region clouds, which are affected by many parameters: ionization equilibrium, density, electron temperature, and extinction. If any of these parameters vary among kinematically distinct structural components of the NLR, line profile variations will result that in turn can help elucidate the NLR structure. An important aspect is that some of these parameters are partially degenerate in infrared datasets: Shorter wavelength (2-5μm) lines which suffer higher extinction are also typically high excitation coronal lines with high critical densities, whereas the longer wavelengths are dominated by ions of lower excitation with transitions with lower critical densities.

Here we have assumed that the observed lines are emitted locally, with no contribution of scattered light. This is not strictly correct for part of the NGC 1068 narrow line region, in particular the NE region (Capetti et al. 1995; Inglis et al. 1995). The impact of scattering on our analysis depends on the properties of the scatterer. If scattering is wavelength-independent, our profile comparison is unaffected since scattering would effectively only redistribute the line emission spatially within our large apertures. If (dust) scattering decreases with wavelength, shorter wavelength line profiles would be modified more strongly. We estimate the effect on the integrated line profiles is not large, since the [O III] polarisations measured by Inglis et al. (1995) reach at most a few percent in regions that are in addition minor contributors to the total flux, and since the considerable spatial variation in line profiles is not suggestive of scattered radiation originating in a central source.

It is unlikely that density variations play a direct role in the profile variations. Our density estimate of $n_e \sim 2000 cm^{-3}$ is too far below the relevant critical densities, making much higher densities over a significant part of the NLR unlikely, which would be required to create the variations. Strictly speaking however, this estimate applies only to the moderately excited (100eV) gas, and our upper limit for the coronal region density is still consistent with densities higher than the critical densities of some lower excitation line. Strong collisional suppression of part of some low critical density fine structure line profiles is also unlikely from the similarity of their line centroids to that of the recombination line Brackett α. We hence believe that the clear correlation of centroid velocities with fine structure line critical density (Figure 8b) is mostly a secondary consequence of the correlation with ionization potential.

Variations in electron temperature can also affect the line profiles. Emissivities of optical forbidden lines like [O III] 5007Å strongly vary with electron temperature while the infrared fine structure lines originate close to the ground state and are much less sensitive to temperature. Hence, at least those profile variations seen among the infrared lines (Figures 7 and 8) must be unrelated to temperature fluctuations. For the optical/IR profile variations there is a basic ambiguity of an optical component being faint due to low electron temperature or due to high extinction. Optical electron temperature determinations e.g. from [O III] 4363Å/5007Å are not available for the various kinematic components of NGC 1068. The line profiles of the temperature insensitive recombination lines in the optical and IR do not resemble each other, but rather follow the shapes of the forbidden optical and IR lines, respectively (Veilleux 1991, Fig. 2). This is inconsistent with temperature variations being the main origin of profile variations.

The exclusion of other factors suggests that ionization structure and extinction are the main source of the observed variation of optical/IR line profiles. Previous studies of the spatial and kinematical structure of the NGC 1068 NLR (e.g. Cecil et al. 1990, Marconi et al. 1996) point to the existence of two spatial and kinematical components. The first is a strong ionization cone with associated blueshifted outflow, with the highest excitation species likely concentrated towards the central and fastest part of this cone. The second is an extended system of photoionized clouds closer to systemic velocity. The correlation between the ISO centroid velocities and the ionization potential (Figure 8a) fits this picture well. If the relative importance of the fast outflow gradually increases towards high excitation lines, the gradual centroid shift is easily explained. However, the marked differences between optical [O III] and infrared [O IV] profile (Figure 6) and the different optical and infrared centroid velocities at similar ionization potential (Figure 8a, including data from Marconi et al. 1996) show that this picture must be incomplete. We suggest that these remaining differences are due to extinction variations across the NLR, with a general trend of higher exctinction in the redshifted (SW) than in the blueshifted (NE) part. The optical profile can be explained by an intrinsic profile similar to that of the IR lines whose line center and red wing are reddened by a few magnitudes, leading to the obscuration of about half of the total line flux. A similar extinction pattern is suggested by the increase of polarization from the blue to the red wing of the *narrow* lines in the central arcseconds (Antonucci & Miller 1985; Bailey et al.

1988; Inglis et al. 1995), attributed to absorption by aligned grains.

Considering that the optical profiles are modified by extinction, it is important to recognize that the less obscured near- and mid-infrared lines remain blueshifted with respect to systemic velocity, high excitation ones more strongly than lower excitation ones. Also, coronal line emission observed in the little obscured near-infrared is still much stronger in the northeast cone than in the southwest (Thompson & Corbin 1999). This might be due to heavy extinction of an intrinsically symmetric NLR, or due to a real asymmetry. No distinction can be made from the present data. A trend with IR extinction is not clear in Figure 8c and would be difficult to separate from the trends with ionization potential and critical density because of the mentioned degeneracy. An intrinsically asymmetric NLR with outflow preferentially towards the observer is fully consistent with the observations of NGC 1068. The difference in strength of the two radio lobes (Wilson & Ulvestad 1983) may be in support of such an asymmetric scenario, although the relation between radio lobe flux and NLR emission is certainly not simple. Consistency with an asymmetric NLR was also noted for the ISO spectra of NGC 4151 (Sturm et al. 1999). However, large randomly oriented AGN samples should not show the preferential blueshift which is noted at least in optical samples. An alternative scenario of a geometrically small but optically highly thick screen (disk or torus) obscuring part of the receding NLR region was proposed by Sturm et al. (1999) for NGC 4151. Such a scenario can also fit the NGC 1068 data provided the screen obscures a relatively larger fraction of the coronal line region than of the larger NLR which is dominated by medium excitation species. This is not implausible given the similar (arcsecond) spatial scale of the central concentration of high column density molecular gas (e.g. Tacconi et al. 1994) and the coronal line region as mapped in [Si VI] (Thompson & Corbin 1999; Thatte et al. 2000). While studies of few individual sources will remain ambiguous, a search for preferential shifts using high resolution near- or mid-infrared spectroscopy should address this issue provided the sample of Seyferts is large enough and not biased by orientation of a putative asymmetric outflow, as may be the case when identifying Seyferts in the optical.

Overall, the structure of the NGC 1068 narrow line region seems to determine the optical/infrared line profiles via differences in weight of outflowing cone and extended components, and additional extinction variations that are significant for the optical wavelength range. The relative weight of the cone is larger for higher excitation species. A tantalizing ambiguity remains that cannot be resolved from a single source study: Is the NLR intrinsically one-sided or is there a very high obscuration screen blocking also part of the IR emission from our view?

5. Molecular hydrogen emission

NGC 1068 was the first galaxy detected in the rovibrational transitions of molecular hydrogen (Thompson et al. 1978) and has been studied since in considerable detail both in these lines tracing fairly excited molecular material (e.g. Oliva & Moorwood 1990; Blietz et al. 1994; Davies et al. 1998), and by millimeter wave interferometry tracing colder components (e.g. Tacconi et al.

1994; Sternberg et al. 1994; Helfer & Blitz 1995; Schinnerer 1999). The system of dense, warm cloud cores in the central few arcseconds inferred from the millimeter studies calls for observations in the pure rotational transitions of molecular hydrogen, which trace gas of typically a few 100K, intermediate between the near-infrared and millimeter wave tracers.

Our SWS observations of these lines (Figure 3, Table 2) are summarized in the H_2 excitation diagram of Figure 9. The diagram has a curved shape suggestive of a mixture of temperatures, as expected from other galaxies observed with ISO in the rotational lines of molecular hydrogen (Rigopoulou et al. 1996; Sturm et al. 1996; Valentijn et al. 1996a; Kunze et al. 1996; Spoon et al. 2000). The location of the S(3) point slightly below the general trend suggests a moderate extinction towards this line whose wavelength is near the center of the silicate absorption feature ($A_{9.6\mu m} \lesssim 1$). As noted earlier, the flux for the heavily blended S(7) line is very uncertain, so that the shorter wavelength rovibrational lines of similar excitation will probably be a more trustworthy representation of the excitation diagram at these upper level energies.

While the higher rotational lines like S(5) and S(7) probe the same excited but low mass component as the near-infrared rovibrational lines, the bulk of the warm gas observed with ISO will reside in the component traced by the S(1) line. In estimating its mass, we will assume a hydrogen ortho/para (O/P) ratio in equilibrium at the local temperature (Sternberg & Neufeld 1999). Combining the S(1) flux with the S(0) limit on one hand and the S(3) detection on the other, the temperature of the S(1) emitting gas is found to lie in the range 140K$\leq$T$\lesssim$375K, assuming the extinction correction for S(3) is modest and aperture effects are minor. Because of the very steep temperature sensitivity of the rotational line emissivities, the corresponding mass varies drastically, between about $4 \times 10^6 M_\odot$ for the 375 K case and $1.5 \times 10^8 M_\odot$ for the 140 K case. For comparison with other mass estimates, we will adopt ~200 K and $\sim 2.5 \times 10^7 M_\odot$ as a possible approximation to the curvature of the excitation diagram. This mass would be of the order 5% of the total gas mass estimated from the CO interferometric map (Helfer & Blitz 1995 and priv. comm.) within the 17μm ISO beam. Compared to a similar estimate for the starburst galaxy NGC 3256 (Rigopoulou et al. 1996, 3% for 150K warm gas temperature), the fraction of warm gas and/or its temperature must be higher, but not exceeding on average that inferred by Kunze et al. (1996) for the highly active star forming region in the 'overlap region' of the antenna galaxies (8% for 200K warm gas temperature).

The NGC 1068 molecular hydrogen emission sampled by SWS may represent a mixture of relatively cool gas from the 15$''$ radius molecular ring partly covered by the longer wavelength apertures, and a warmer component from the unusually dense and warm central few arcseconds (Tacconi et al. 1994; Blietz et al. 1994). Knowing from the S(3) measurement that the extinction to the H_2 emitting region cannot be very large, we can compare our 1-0 Q(3) flux to 1-0 S(1) fluxes measured in smaller apertures (1.4 to 2.2×10^{-20}W cm^{-2}; Blietz et al. 1994; Thompson et al. 1978). Our Q(3) line flux falls in the middle of that range. Since the intrinsic Q(3)/S(1) flux ratio is 0.7, the implication is that the central few arcseconds dominate at least for the more highly excited hydrogen lines, though there may be some extended contribution. Some of the molecular hydrogen emission in NGC 1068 may originate in X-ray irradiated gas. We include in Table 2 upper limits for two transitions of H_3^+ which have been proposed as a signature of X-ray heated molecular gas (Draine & Woods 1990). We note, however, that these limits are not at all stringent and are fully consistent with even the 'high' end of H_3^+ flux expectations for X-ray illumination. Estimates are uncertain, see e.g. the much lower predictions of Maloney et al. (1996).

The question can be raised whether the NGC 1068 H_2 spectra in fact contain a direct signature of a parsec-scale molecular torus. Krolik and Lepp (1989) have modelled molecular line emission of such an X-ray illuminated torus, predicting emission in some molecular hydrogen lines like (0-0) S(5) that may under favorable conditions be detectable at ISO-SWS sensitivities. For NGC 1068 it is evident that larger scale emission may swamp any possible torus emission, as already cautioned by Krolik and Lepp (1989). The ISO data smoothly complement the near-infrared emission originating in larger scale (~100pc) clouds, following an excitation diagram plausibly ascribed to the same clouds. If any torus emission were present at lower level, it may be difficult to discriminate from the larger scale emission since, depending on black hole mass and spatial scale, its velocity width could be very similar to the larger scale emission. The widths of our H_2 rotational lines are consistent with those for CO observed on 100pc and larger scales, with no evidence for other kinematic components. However, even if the rotational emission does not trace a compact torus, it may still be excited to a significant fraction by UV radiation, X-rays or shocks related to the AGN.

6. Summary

ISO-SWS spectroscopy provides the first detailed census of the mid-infrared spectrum of the prototypical Seyfert 2 galaxy NGC 1068. We have detected 36 emission lines on top of the strong AGN-heated continuum. Most lines originate in the NLR characterized by a density of $\sim 2000\,\mathrm{cm}^{-3}$.

We have compared the mid-infrared ISO line profiles with optical emission line profiles produced in the NLR. The line profiles are consistent with a model where the NLR is a combination of a highly ionized outflow and lower excitation extended emission, with extinction significantly affecting the optical line profiles. Remaining blueshift and asymmetry of the least obscured lines may reflect either intrinsic asymmetry of the NLR or an additional very high column density obscuring component.

We detect strong emission from warm molecular hydrogen, which most likely originates on the 100pc to kpc scale, and which is also probed by emission in near-infrared and millimeter wave tracers of molecular material. This emission masks any possible emission from a putative parsec-scale molecular torus.

Companion papers use the SWS data to model the spectral energy distribution of the active nucleus, to put limits on emission from the obscured broad line region, and discuss the continuum and its features.

We are grateful to Eike Guenther and Shai Kaspi for obtaining optical spectra that were invaluable in the interpretation of the ISO spectra, and to Richard Pogge and M.M. de Robertis for providing us with an unpublished [O III] image of NGC 1068. SWS and the ISO Spectrometer Data Center at MPE are supported by DLR (DARA) under grants 50 QI 8610 8 and 50 QI 9402 3. We acknowledge support by the German-Israeli Foundation (grant I-0551-186.07/97).

REFERENCES

Alexander T., Sturm E., Lutz D., Sternberg A., Netzer H., Genzel R. 1999, ApJ, 512, 204

Alexander T., et al., submitted to ApJ

Alloin D., Pelat D., Boksenberg A., Sargent W.L.W. 1983, ApJ, 275, 493

Antonucci R.R.J., Miller J.S. 1985, ApJ, 297, 621

Appenzeller I., Östreicher R. 1988, AJ, 95, 45

Axon D.J., Marconi A., Capetti A., Macchetto F.D., Schreier E., Robinson A., 1998, ApJ, 496, L75

Bailey J., Axon D.J., Hough J.H., Ward M.J., McLean I., Heathcote S.R. 1988, MNRAS, 234, 899

Blietz M., Cameron M., Drapatz S., Genzel R., Krabbe A., van der Werf P., Sternberg A., Ward M. 1994, ApJ, 421, 92

Bock J.J., Marsh K.A., Ressler M.E., Werner M.W. 1998, ApJ, 504, L5

Braatz J.A., Wilson A.S., Gezari D.Y., Varosi F., Wilson A.S. 1993, ApJ, 409, L5

Brinks E., Skillman E.D., Terlevich R.D., Terlevich E. 1997, Ap&SS, 248, 31

Cameron M., Storey J.W.V., Rotaciuc V., Genzel R., Verstraete L., Drapatz S., Siebenmorgen R., Lee T.J. 1993, ApJ, 419, 136

Capetti A., Axon D.J., Macchetto F., Sparks W.B., Boksenberg A. 1995, ApJ, 446, 155

Cecil G., Bland J., Tully R.B. 1990, ApJ, 355, 70

Dahari O., De Robertis M.M. 1988, ApJ, 331, 727

Davies R., Sugai H., Ward M.J. 1998, MNRAS, 300, 388

De Robertis M.M., Osterbrock D. 1986, ApJ, 301, 727

Dietrich M., Wagner S.J. 1998, A&A, 338, 405

Draine B.T. 1989, in: "Proc. 22nd Eslab Symposium on Infrared Spectroscopy in Astronomy", ESA SP-290, (Noordwijk: ESA), 93

Draine B.T., Woods D.T. 1990, ApJ, 363, 464

Evans I.N., Ford H.C., Kinney A.L., Antonucci R.R.J., Armus L., Caganoff S., 1991, ApJ, 369, 27

Feuchtgruber H., et al. 1997, ApJ, 487, 962

Förster-Schreiber N. 1998, PhD Thesis, Ludwig-Maximilians-Universität München

Genzel R., et al. 1998, ApJ, 498, 579

Glass I.S. 1997, Ap&SS, 248, 191

de Graauw Th., et al. 1996, A&A, 315, L49

Heckman T.M., Miley G.K., van Breugel W.J.M., Butcher H.R. 1981, ApJ, 247, 403

Helfer T.T., Blitz L. 1995, ApJ, 450,90

Hummer D.G., Storey P.J. 1987, MNRAS, 224, 801

Inglis M.D., Young S., Hough J.H., Gledhill T., Axon D.J., Bailey J.A., Ward M.J. 1995, MNRAS, 275, 398

Kessler M.F., et al. 1996, A&A, 315, L27

Koski A.T. 1978, ApJ, 223, 56

Krolik J.H., Begelman M.C. 1988, ApJ, 329, 702

Krolik J.H., Lepp S. 1989, ApJ, 347, 149

Kunze D., et al. 1996, A&A, 315, L101

Lahuis F., et al. 1998, in Astronomical Data Analysis Software and Systems VII, A.S.P. Conference Series, Vol. 145, eds. R. Albrecht, R.N. Hook and H.A. Bushouse, p.224

Lebofsky M.J., Rieke G.H., Kemp J.C. 1978, ApJ, 222,98

Lutz D., et al. 1996, A&A, 315, L269

Lutz D., Sturm E., Genzel R., Moorwood A.F.M., Sternberg A. 1997, Ap&SS, 248, 217

Lutz D., et al. 1997, in: "First ISO Workshop on Analytical Spectroscopy", eds. A.M. Heras et al., ESA-SP419 (Noordwijk:ESA), 143

Lutz D., et al. 2000, ApJ, in press

Macchetto F., Capetti A., Sparks W.B., Axon D.J., Boksenberg A. 1994, ApJ, 435, L15

Maloney P.R., Hollenbach D.J., Tielens A.G.G.M. 1996, ApJ, 466, 561

Marconi A., van der Werf P.P., Moorwood A.F.M., Oliva E. 1996, A&A, 315, 335

Meaburn J., Pedlar A. 1986, A&A, 159, 336

Moorwood A.F.M., Lutz D., Oliva E., Marconi A., Netzer H., Genzel R., Sturm E., de Graauw Th. 1996, A&A, 315, L109

Myers S.T., Scoville N.Z. 1987, ApJ, 312, L39

Oliva E., Moorwood A.F.M. 1990, ApJ, 348, L5

Pécontal E., Ferruit P., Binette L., Wilson A.S. 1997, Ap&SS, 248, 167

Pelat D., Alloin D. 1980, A&A, 81, 172

Pelat D., Alloin D., Fosbury R.A.E 1981, MNRAS, 195, 787

Penston M.V., Fosbury R.A.E., Boksenberg A., Ward M.J., Wilson A.S. 1984, MNRAS, 208, 347

Pier E.A., Krolik J.H. 1992, ApJ, 401, 99

Pogge R.W. 1988, ApJ, 328, 519

Rieke G.H., Low F.J. 1975, ApJ, 199, L13

Rigopoulou D., et al. 1996, A&A, 315, L125

Roelfsema P.R., et al. 1996, A&A, 315, L289

Schaeidt S.G., et al. 1996, A&A, 315, L55

Schinnerer E. 1999, PhD Thesis, Ludwig-Maximilians-Universität München

Shields G.A., Oke J.B. 1975, ApJ, 197, 5

Spinoglio L., Malkan M.A. 1992, ApJ, 399, 504

Spoon H.W.W., et al. 2000, submitted to A&A

Sternberg A., Genzel R., Tacconi L. 1994, ApJ, 436, L131

Sternberg A., Neufeld D. 1999, ApJ, 520, 137

Sturm E., et al. 1996, A&A, 315, L133

Sturm E., Alexander T., Lutz D., Sternberg A., Netzer H., Genzel R. 1999, ApJ, 512, 197

Sturm E., et al. 2000, in preparation

Tacconi L.J., Genzel R., Blietz M., Cameron M., Harris A.I., Madden S. 1994, ApJ, 426, L77

Telesco C.M., Decher R. 1998, ApJ, 334, 573

Thatte N., Quirrenbach A., Genzel R., Maiolino R., Tecza M. 1997, ApJ, 490, 238

Thatte N. et al., 1999, in preparation

Thompson R.I., Lebofsky M.J., Rieke G.H. 1987, ApJ, 222, L49

Thompson R.I., Corbin M. 1999, Ap&SS, in press (Proceedings of Ringberg workshop on ultraluminous infrared galaxies)

Tully R.B. 1988, Nearby Galaxies Catalog (Cambridge: Cambridge University Press)

Unger S.W., Lewis J.R., Pedlar A., Axon D.J. 1992, MNRAS, 258, 371

Valentijn E.A., et al. 1996, A&A, 315, L60

Valentijn E.A., van der Werf P.P., de Graauw Th., de Jong T. 1996, A&A, 315, L145

Veilleux S. 1991, ApJS, 75, 357

Vrtilek J.M., Carleton N.P. 1985, ApJ, 294, 106

Walker M.F. 1968, ApJ, 151, 71

Wieprecht E., et al. 1998, in Astronomical Data Analysis Software and Systems VII, A.S.P. Conference Series, Vol. 145, eds. R. Albrecht, R.N. Hook and H.A. Bushouse, p.279

Whittle M. 1985a, MNRAS, 213, 1

Whittle M. 1985b, MNRAS, 216, 817

Wilson A.S., Ulvestad J.S. 1983, ApJ, 275, 8

This preprint was prepared with the AAS LaTeX macros v4.0.

Table 1: Journal of SWS observations of NGC 1068

Revolution	Date UT	AOT	Duration s	Slit Position angle °
285	28-Aug-1996	SWS01	6538	-11
285	28-Aug-1996	SWS02	3212	-11
605	13-Jul-1997	SWS06	4080	-23
633	10-Aug-1997	SWS06	8410	-16
643	20-Aug-1997	SWS06	5710	-13
788	12-Jan-1998	SWS06	7766	157
788	12-Jan-1998	SWS02	1990	157
792	15-Jan-1998	SWS06	14642	158
806	29-Jan-1998	SWS06	11810	162
818	11-Feb-1998	SWS06	2134	165

Table 2: NGC 1068 emission lines measured with ISO-SWS

Line	$\lambda_{rest,vac}$	E_{Ion}[a]	Flux	Meth[b]	Aperture	Velocity[c]
	μm	eV	10^{-20} W cm^{-2}		$'' \times ''$	km/s
H_2 (1-0) Q(3)	2.424	0.0	1.7	i	14×20	1140
[Si IX]	2.584	303.2	3.0	f	14×20	
Br β, H_2 (1-0) O(2)	2.626	13.6	4.1[d]	f	14×20	
[Mg VIII]	3.028	224.9	11.0	f	14×20	1000
[Ca IV]	3.207	50.9	1.3	f	14×20	
H_2 (1-0) O(5)	3.235	0.0	0.8	i	14×20	1120
Pf γ	3.741	13.6	<4.0	u	14×20	
[Si IX]	3.936	303.2	5.4	f	14×20	950
Br α	4.052	13.6	6.9	f	14×20	1110
$H_3^+ 1,2,3_{+1} \rightarrow 3,3$	4.350	0.0	<3.0	u	14×20	
[Mg IV]	4.487	80.1	7.4	f	14×20	
[Ar VI]	4.530	75.0	15.0	f	14×20	
Pf β	4.654	13.6	<10.0	u	14×20	
[Na VII]	4.685	172.1	<11.0	u	14×20	
H_2 (0-0) S(9)	4.695	0.0	<3.5	u	14×20	
[Fe II]	5.340	7.9	5.0	i	14×20	1120
[Mg VII]	5.503	186.5	13.0	s	14×20	
H_2 (0-0) S(7)	5.511	0.0	3.5::	s	14×20	
[Mg V]	5.610	109.2	18.0	f	14×20	
H_2 (0-0) S(5)	6.910	0.0	5.9	i	14×20	1180
[Ar II]	6.985	15.8	13.0	i	14×20	
[Na III]	7.318	47.3	5.8	f	14×20	
Pf α	7.460	13.6	<3.0	u	14×20	
Unidentified	~7.555	—	1.8	f	14×20	
[Ne VI]	7.652	126.2	110.0	f	14×20	1030
[Fe VII]	7.815	99.1	3.0	f	14×20	
[Ar V]	7.902	59.8	<12.0	u	14×20	
H_2 (0-0) S(4)	8.025	0.0	3.5	i	14×20	1130
[Na VI]	8.611	138.4	<16.0	u	14×20	
[Ar III]/[Mg VII]	8.991	27.6/186.5	25.0	f	14×20	
[Fe VII]	9.527	99.1	4.0	f	14×20	
H_2 (0-0) S(3)	9.665	0.0	6.0	i	14×20	1130
[S IV]	10.511	34.8	58.0	f	14×20	
H_2 (0-0) S(2)	12.279	0.0	<8.0	u	14×27	
[Ne II]	12.814	21.6	70.0	i	14×27	1080
[Ar V]	13.102	59.8	<16.0	u	14×27	
[Ne V]	14.322	97.1	97.0	f	14×27	1020
[Ne III]	15.555	41.0	160.0	f	14×27	1090
$H_3^+ 5,0 \rightarrow 4,3$	16.331	0.0	<6.0	u	14×27	
H_2 (0-0) S(1)	17.035	0.0	7.7	i	14×27	1120
[Fe II]	17.936	7.9	<10.0	u	14×27	
[S III]	18.713	23.3	40.0	i	14×27	1120
[Ne V]	24.318	97.1	70.0	f	14×27	1060
[O IV]	25.890	54.9	190.0	f	14×27	1100
[Fe II]	25.988	7.9	8.0::	s	14×27	
H_2 (0-0) S(0)	28.219	0.0	<2.5	u	20×27	
[S III]	33.418	23.3	55.0	i	20×33	1110
[Si II]	34.815	8.2	91.0	i	20×33	1110
[Ne III]	36.014	41.0	18.0	f	20×33	

[a] Lower ionization potential of the stage leading to the transition

[b] Method of flux measurement: f = fit of double-gaussian NLR profile, i = direct integration, u = 3σ upper limit assuming a line width of 1000km/s (ions) or 300km/s (molecules), s = special fit. See also text.

[c] Heliocentric velocity determined from fitting a single gaussian plus continuum to the – sometimes complex – line profile.

[d] Brackett β is blended with H_2 (1-0) O(2). From the (1-0) Q(3) and (1-0) O(5) fluxes, we estimate a (1-0) O(2) contribution of $\sim 0.4 \times 10^{-20}$ W cm^{-2} to the total flux

Fig. 1.— Complete 2.4–45μm ISO-SWS spectrum of NGC 1068. Some of the brightest emission lines are indicated.

Fig. 2.— ISO-SWS spectra of lines emerging in the ionized medium of NGC 1068. Flux densities in Jy are shown for a range of $\pm$2500 km/s around systemic velocity. Most lines originate in the narrow line region but some low excitation lines have a significant starburst contribution. The two lines shown dashed were observed in SWS01 mode, all others in full resolution SWS06 mode.

Fig. 3.— ISO-SWS spectra of molecular transitions in NGC 1068. Flux densities in Jy are shown for a range of $\pm$1000 km/s around systemic velocity. The line shown dashed was observed in SWS01 mode, all others in full resolution SWS02 or SWS06 modes.

Fig. 4.— Normalized line profiles for five high signal to noise fine structure lines in NGC 1068, covering a range of lower ionization potentials from 55 to 303eV. The velocity scale is with respect to the heliocentric systemic velocity of 1148 km/s. Short lines in the upper right part of the panels indicate the SWS resolution at that wavelength. In the lower right panel, we show a combination of two gaussians which provides a reasonable approximation to the mid-infrared NLR line profiles over this wide range of ionization potentials. We have used fits of such a profile to measure *fluxes* of fainter lines.

Fig. 5.— Comparison of the large aperture [O III] 5007Å profile obtained at Karl Schwarzschild Observatory with the smaller aperture one of Veilleux (1991). The velocity scale is with respect to the heliocentric systemic velocity of 1148 km/s - note that this differs from the original figure of Veilleux (1991). The dashed line indicates a suggested extrapolation of the KSO spectrum to the larger ISO aperture of $14'' \times 20''$, taking into account extended narrow emission near systemic velocity, mainly from the NE region of the NLR. See text for details.

Fig. 6.— Comparison of the infrared [O IV] and optical [O III] line profiles. The peak of the optical profile is normalized to 1, 0.8, 0.6, and 0.4 times the peak of the infrared profile in the four panels. The optical profile is the modified KSO profile of Figure 5 smoothed to the SWS resolution at the wavelength of [O IV]. While many structures are present in both optical and infrared profile, there

are pronounced differences in the relative strengths of center and blue/red wings.

Fig. 7.— Direct comparison of the four highest signal-to-noise fine structure line profiles. The velocity scale is with respect to the heliocentric systemic velocity of 1148 km/s.

Fig. 8.— Centroid velocities for NGC 1068 emission lines, derived from fits of a single gaussian. Systemic velocity is indicated by the dashed line in the upper left panel. The correlation with ionization potential includes all ISO lines with a velocity listed in Table 2 (crosses) with the addition of the optical [O III] line (shown as an asterisk in all graphs). For comparison with the ISO mid-infrared results, centroid velocities of optical/near-infrared lines as derived by Marconi et al. (1996) are shown as small diamonds in the upper left panel. The graphs showing velocity as a function of critical density and of extinction are restricted to lines dominated by the NLR according to the line profile. The velocities shown are accurate to $\lesssim$50km/s.

Fig. 9.— Excitation diagram for the molecular hydrogen lines measured with SWS in NGC 1068.

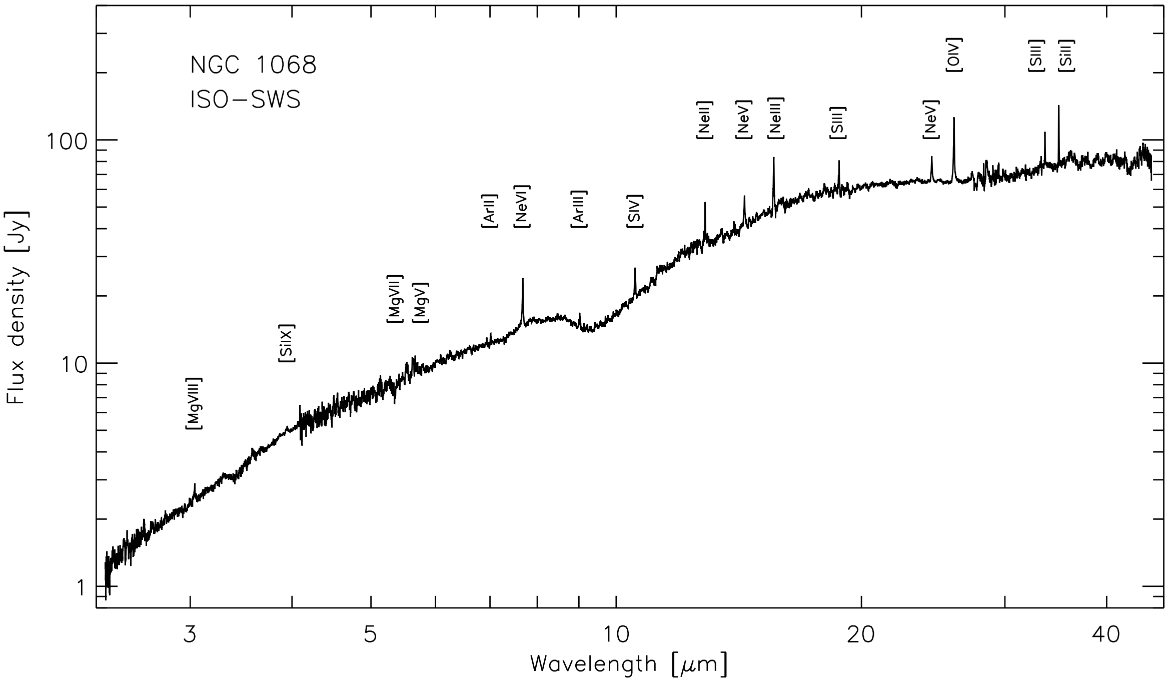
NGC 1068
ISO–SWS
[MgVIII]
[SiIX]
[MgVII]
[MgV]
[ArII]
[NeVI]
[ArIII]
[SIV]
[NeII]
[NeV]
[NeIII]
[SIII]
[NeV]
[OIV]
[SIII]
[SiII]
Flux density [Jy]
Wavelength [μm]
1
10
100
3
5
10
20
40

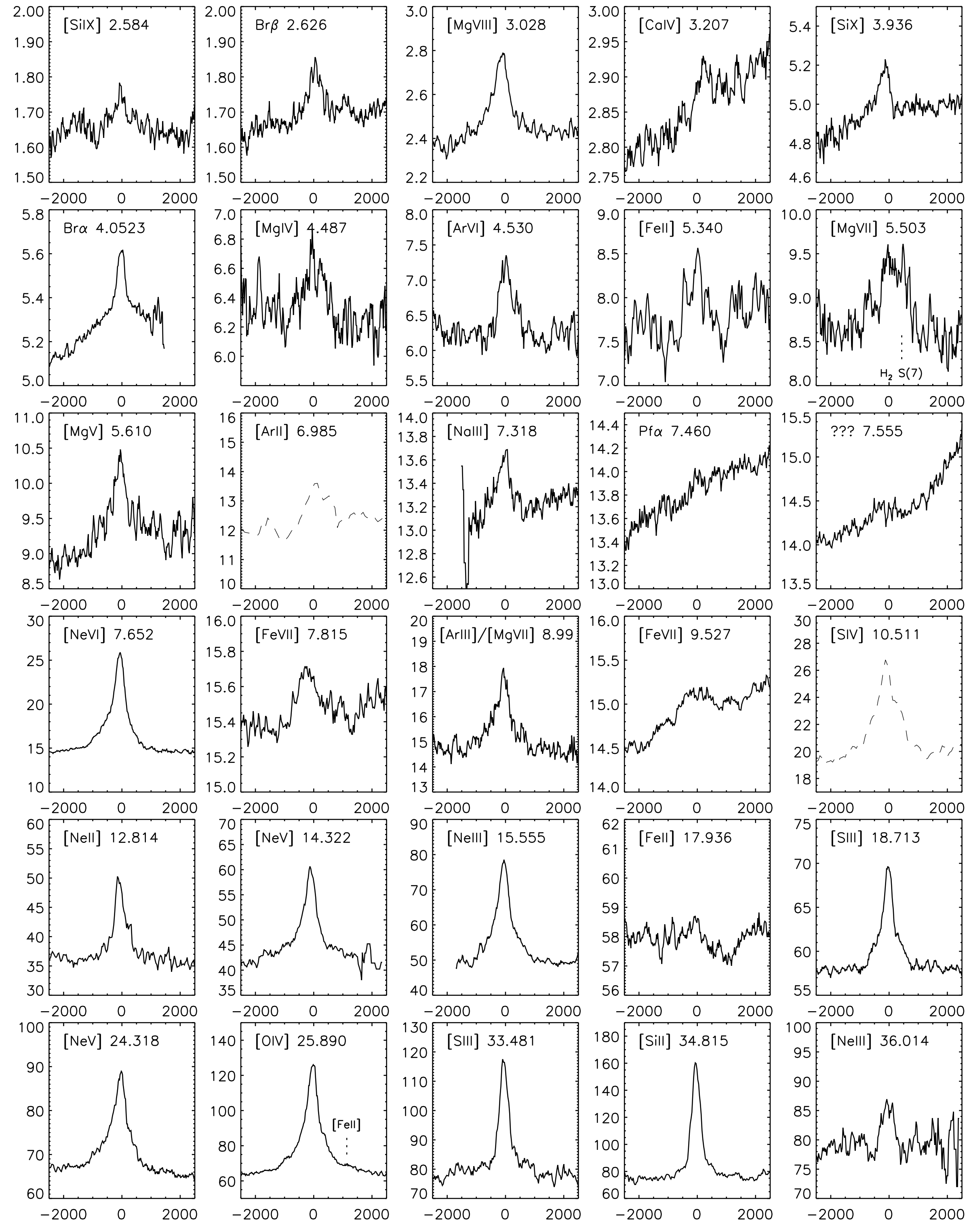
[SiIX] 2.584
Brβ 2.626
[MgVIII] 3.028
[CaIV] 3.207
[SiX] 3.936
Brα 4.0523
[MgIV] 4.487
[ArVI] 4.530
[FeII] 5.340
[MgVII] 5.503
H2 S(7)
[MgV] 5.610
[ArII] 6.985
[NaIII] 7.318
Pfα 7.460
??? 7.555
[NeVI] 7.652
[FeVII] 7.815
[ArIII]/[MgVII] 8.99
[FeVII] 9.527
[SIV] 10.511
[NeII] 12.814
[NeV] 14.322
[NeIII] 15.555
[FeII] 17.936
[SIII] 18.713
[NeV] 24.318
[OIV] 25.890
[FeII]
[SIII] 33.481
[SiII] 34.815
[NeIII] 36.014

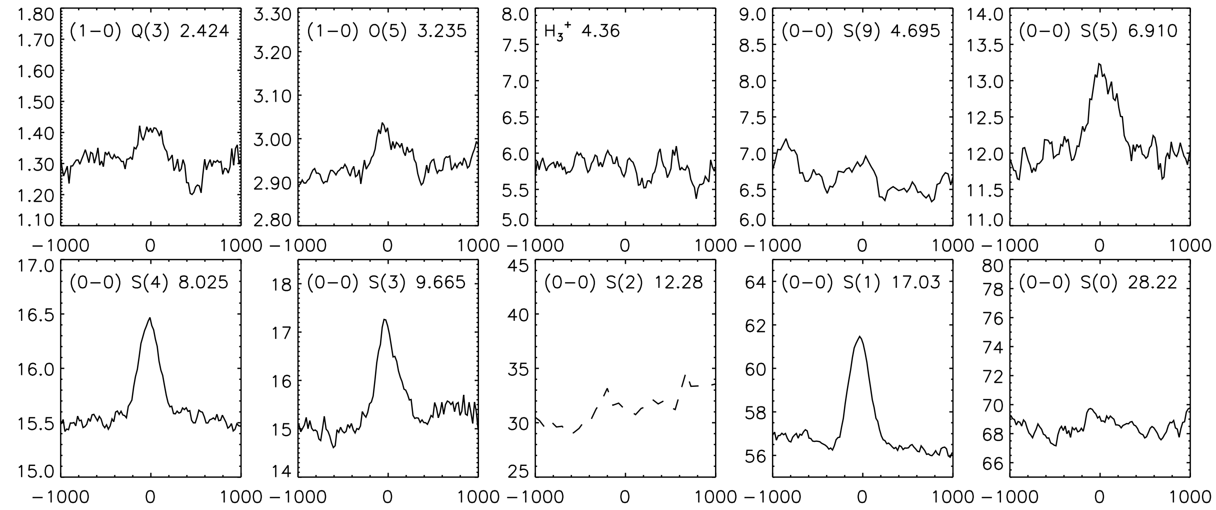
(1–0) Q(3) 2.424
(1–0) O(5) 3.235
H_3^+ 4.36
(0–0) S(9) 4.695
(0–0) S(5) 6.910
(0–0) S(4) 8.025
(0–0) S(3) 9.665
(0–0) S(2) 12.28
(0–0) S(1) 17.03
(0–0) S(0) 28.22

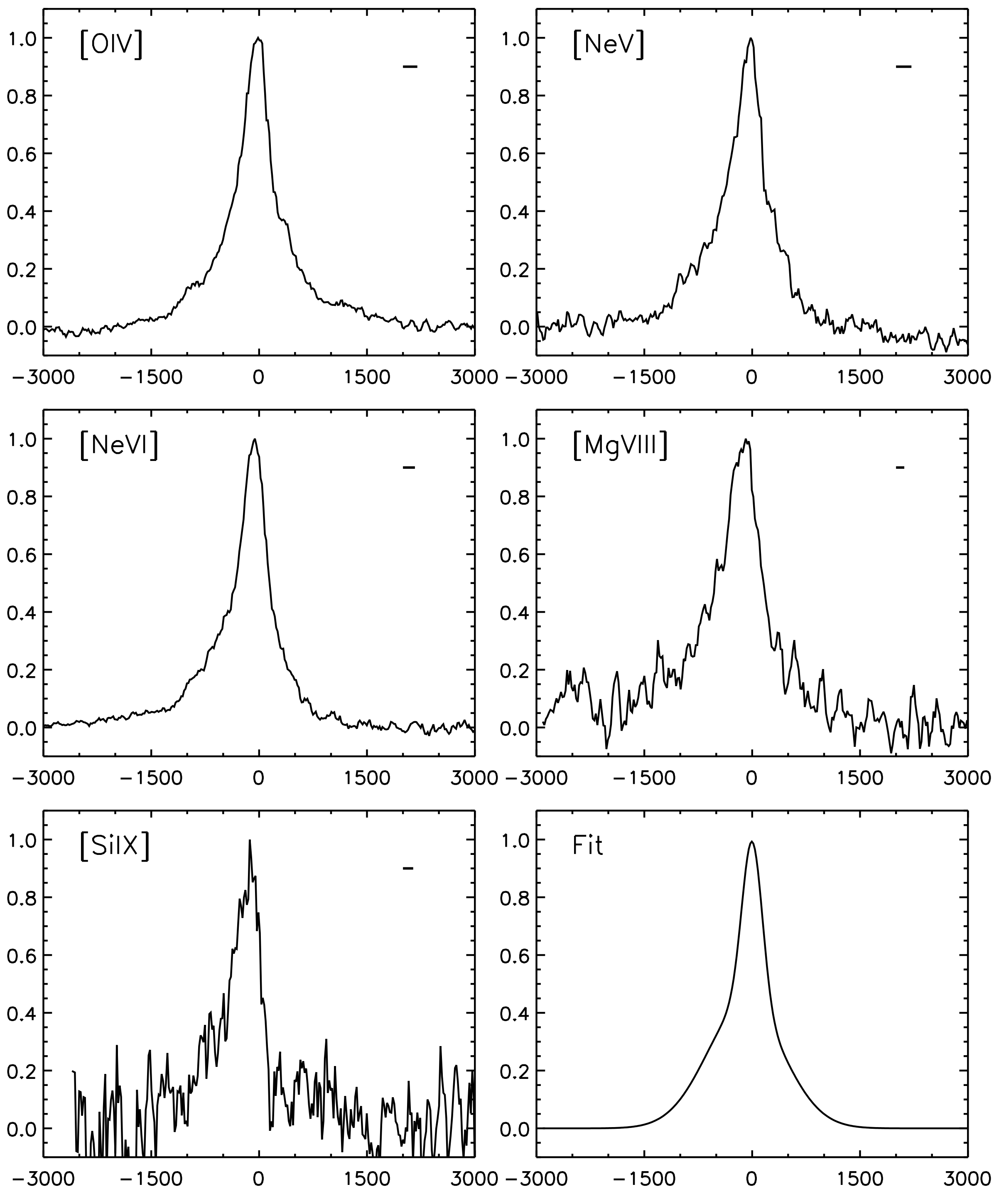
[OIV]
[NeV]
[NeVI]
[MgVIII]
[SiIX]
Fit
1.0
0.8
0.6
0.4
0.2
0.0
−3000
−1500
0
1500
3000

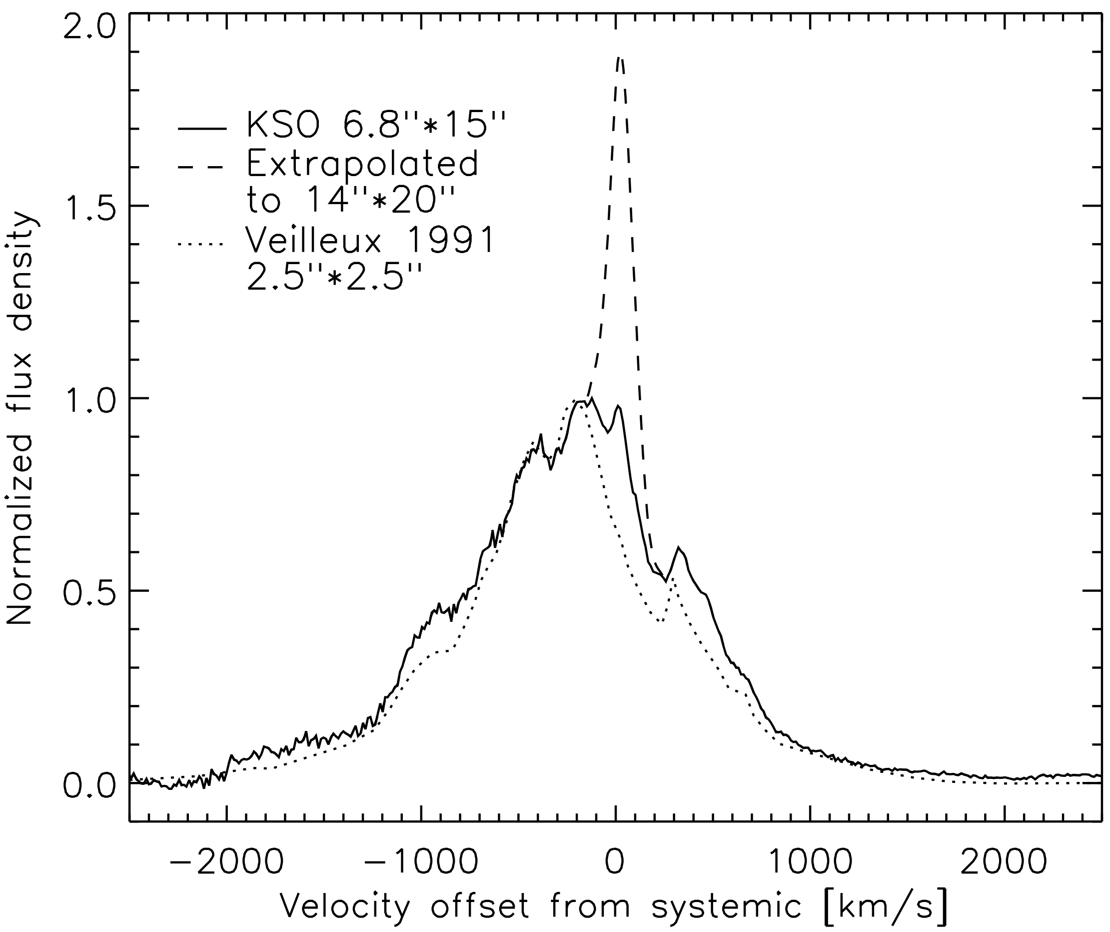
KSO 6.8''*15''
Extrapolated
to 14''*20''
Veilleux 1991
2.5''*2.5''
Normalized flux density
Velocity offset from systemic [km/s]
2.0
1.5
1.0
0.5
0.0
−2000
−1000
0
1000
2000

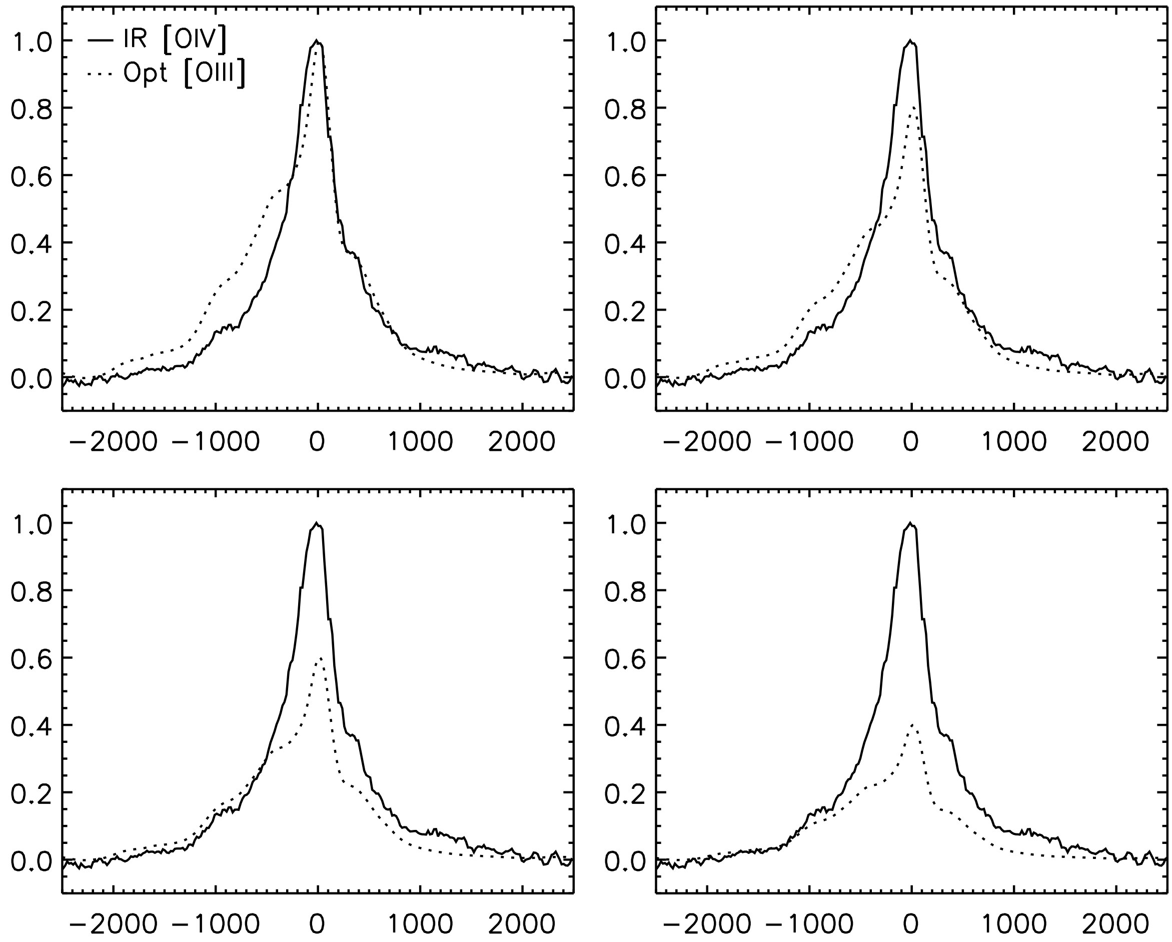

— IR [OIV]
··· Opt [OIII]

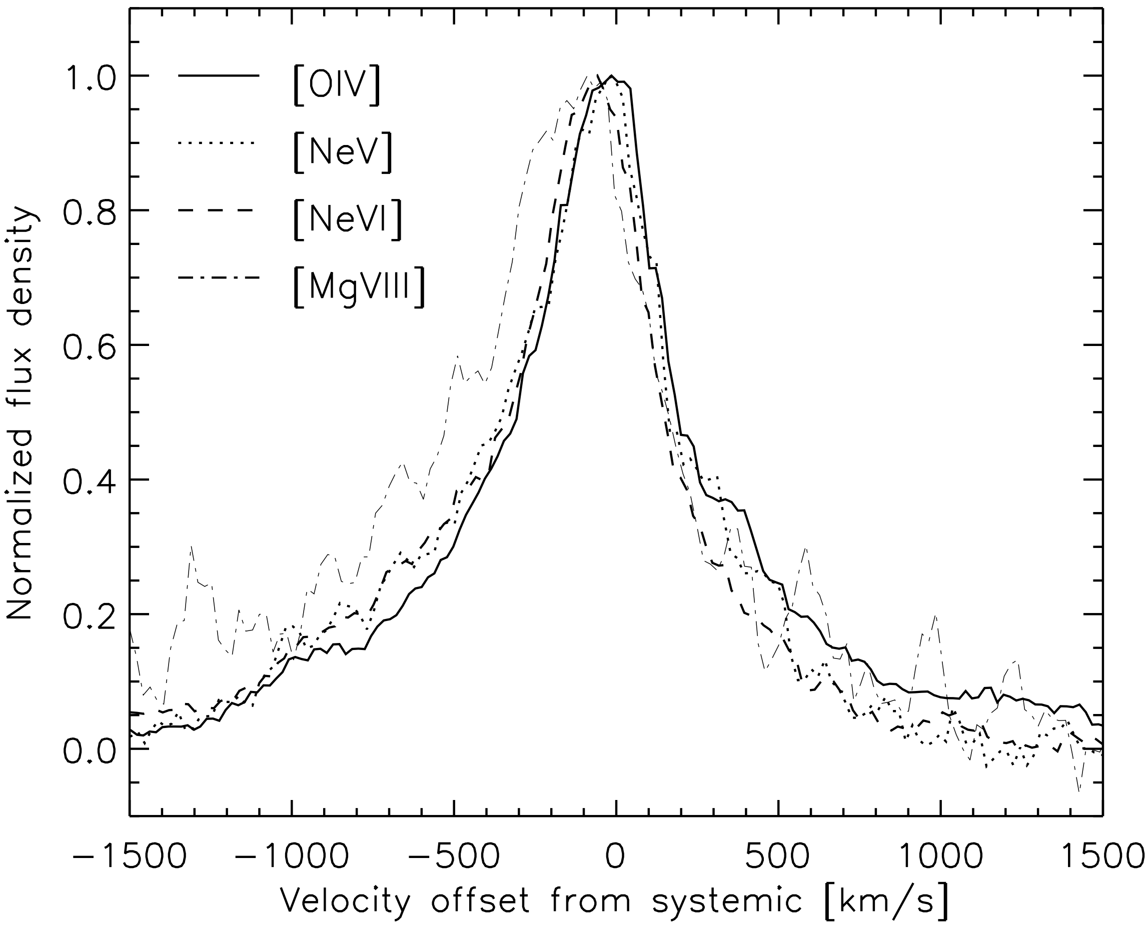
[OIV]
[NeV]
[NeVI]
[MgVIII]
1.0
0.8
0.6
0.4
0.2
0.0
Normalized flux density
−1500
−1000
−500
0
500
1000
1500
Velocity offset from systemic [km/s]

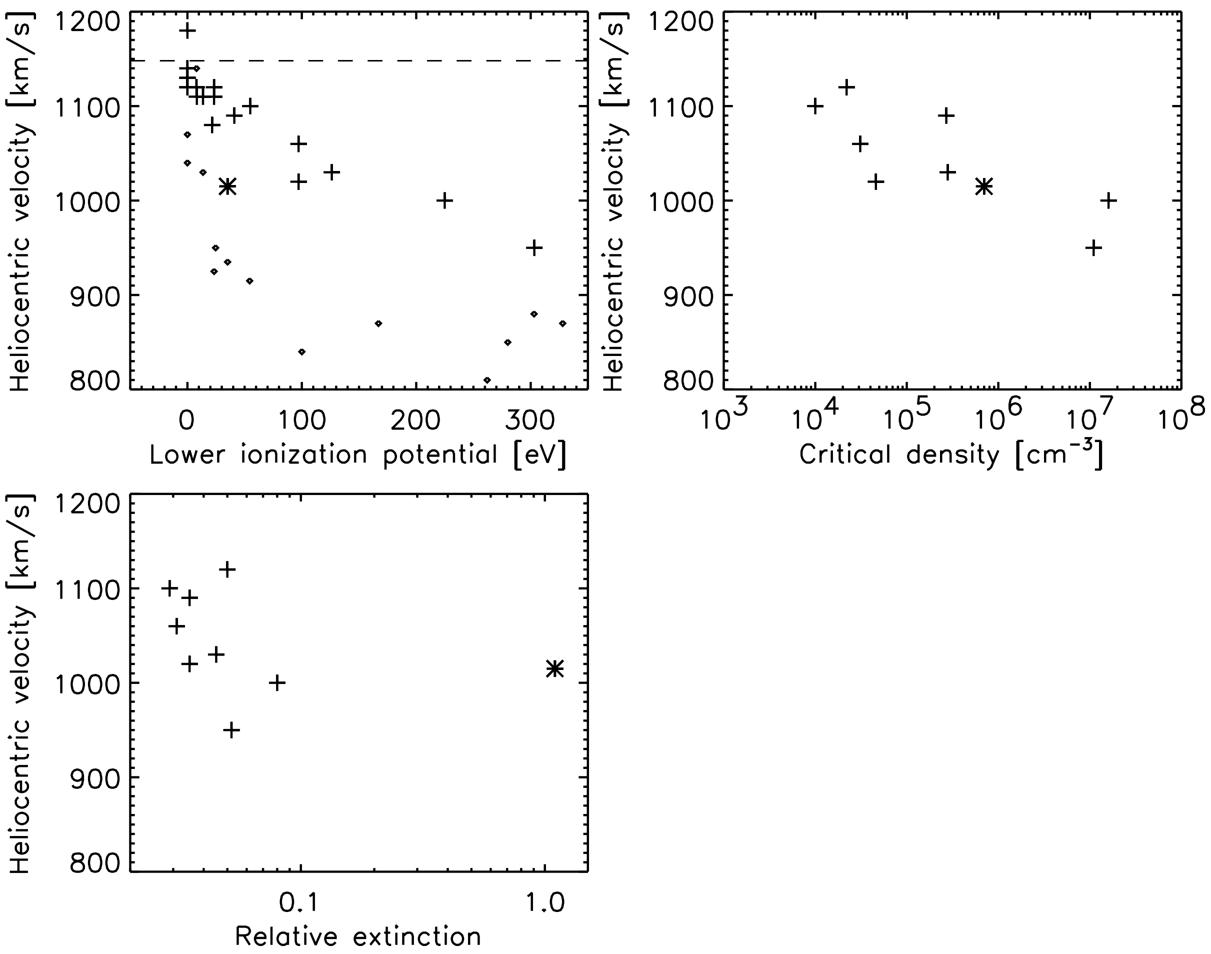

Heliocentric velocity [km/s]
1200
1100
1000
900
800
0
100
200
300
Lower ionization potential [eV]
10^3
10^4
10^5
10^6
10^7
10^8
Critical density [cm^{-3}]
0.1
1.0
Relative extinction

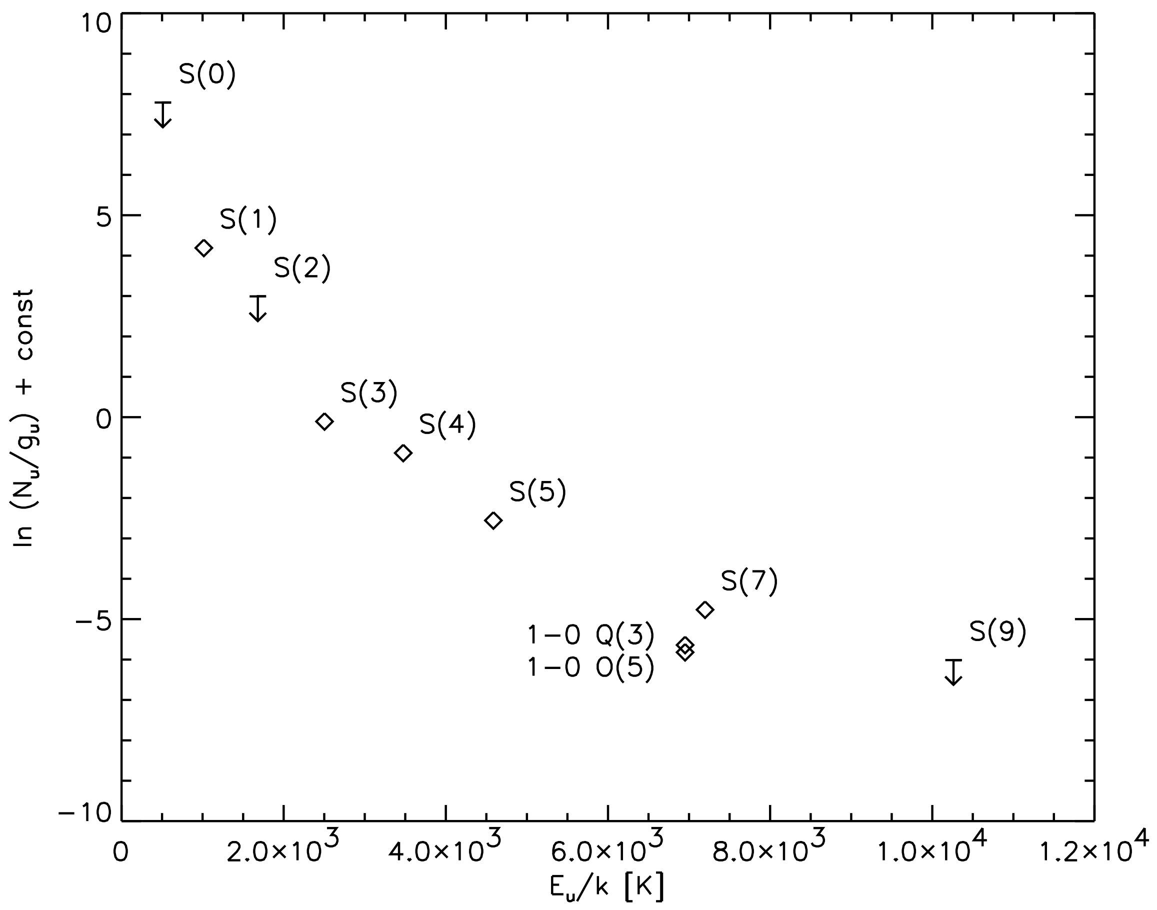
S(0)
S(1)
S(2)
S(3)
S(4)
S(5)
S(7)
1−0 Q(3)
1−0 O(5)
S(9)
ln (N_u/g_u) + const
E_u/k [K]
10
5
0
−5
−10
0
2.0×10^3
4.0×10^3
6.0×10^3
8.0×10^3
1.0×10^4
1.2×10^4